Fast image-formation algorithm for ultrahigh-resolution airborne squint spotlight synthetic aperture radar based on adaptive sliding receive-window technique

Wei Yang
Hong-cheng Zeng
Jie Chen
Peng-bo Wang

Fast image-formation algorithm for ultrahigh-resolution airborne squint spotlight synthetic aperture radar based on adaptive sliding receive-window technique

Wei Yang, Hong-cheng Zeng, Jie Chen,* and Peng-bo Wang
Beihang University, School of Electronics and Information Engineering,
Xueyuan Road 37, Beijing 100191, China

Abstract. Adaptive sliding receive-window (ASRW) technique was usually introduced in airborne squint synthetic aperture radar (SAR) systems. Airborne squint spotlight SAR varies its receive-window starting time pulse-by-pulse as a function of range-walk, namely, the linear term of range cell migration (RCM). As a result, a huge data volume of the highly squint spotlight SAR echo signal can be significantly reduced. Because the ASRW technique changes the echo-receive starting time and Doppler history, the conventional image algorithm cannot be employed to directly focus airborne squint spotlight ASRW-SAR data. Therefore, a fast image-formation algorithm, based on the principle of the wave number domain algorithm (WDA) and azimuth deramping processing, was proposed for accurately and efficiently focusing the squint spotlight ASRW-SAR data. Azimuth deramping preprocessing was implemented for eliminating azimuth spectrum aliasing. Moreover, bulk compression and modified Stolt mapping were utilized for high-precision focusing. Additionally, geometric correction was employed for compensating the image distortion resulting from the ASRW technique. The proposed algorithm was verified by evaluating the image performance of point targets in different squint angles. In addition, a detailed analysis of computation loads in the appendix indicates that the processing efficiency can be greatly improved, e.g., the processing efficiency could be improved by 17 times in the 70-deg squint angle by applying the proposed image algorithm to the squint spotlight ASRW-SAR data. © *The Authors. Published by SPIE under a Creative Commons Attribution 3.0 Unported License. Distribution or reproduction of this work in whole or in part requires full attribution of the original publication, including its DOI.* [DOI: 10.1117/1.JRS.8.083620]

1 Introduction

Synthetic aperture radar (SAR) plays a significant role in remote sensing.[1–3] Recently, airborne squint spotlight SAR has become one of the most important topics in microwave remote sensing, as it has the advantages of illuminating a particular area within a single pass of the platform by foreword/backward-squinted antenna and providing higher azimuth resolution by operating at a spotlight mode.[4,5] Therefore, squint spotlight SAR currently has significant applications in intelligence surveillance, security monitoring, target detection, etc.[6,7]

However, the state-of-the-art ultrahigh-resolution airborne squint spotlight SAR has to deal with an extremely huge volume of raw data due to the large range cell migration (RCM) that results from the highly squinted angle and high-signal sampling rate corresponding to a high-range resolution. As a result, it leads to higher computation loads and lower efficiency in SAR image formation processing. In this article, the adaptive sliding receive-window (ASRW) technique was introduced for effectively reducing RCM in a -squinted airborne spotlight SAR system. In this system, its receive-window starting time varies pulse-by-pulse as a function of range-walk, namely, the linear term of RCM. Consequently, both data volume and

---

*Address all correspondence to: Jie Chen, E-mail: chenjie@buaa.edu.cn

computation loads can be significantly reduced. As a consequence the squint SAR system makes real-time processing feasible, especially for the intelligence reconnaissance airborne SAR system. However, those classical squint SAR data image algorithms, such as the nonlinear chirp-scaling algorithm, extended nonlinear chirp-scaling algorithm, and wave number domain algorithm (WDA),[8-11] cannot be employed to focus squint spotlight ASRW-SAR data directly for not considering the sliding receive-window effects.

In this article, a fast image-formation algorithm for ultrahigh-resolution airborne squint spotlight ASRW-SAR was proposed based on the principle of WDA and the azimuth deramping technique. Azimuth deramping preprocessing was implemented for eliminating azimuth spectrum aliasing.[12] Moreover, WDA is a good method for focusing squint spotlight SAR data because of its high accuracy and efficiency.[1,13] In the WDA part, bulk compression and modified Stolt mapping were utilized for implementing high-precision focusing. Geometric correction was also employed for compensating the geometric distortion that results from the ASRW technique.

In this article, Sec. 2 analyzes the airborne squint spotlight SAR in detail using the ASRW technique. Subsequently, a fast image-formation algorithm for airborne squint spotlight ASRW-SAR was proposed in Sec. 3. Then, the point targets simulation experiments were carried out in Sec. 4 to prove the validity of the proposed algorithm, and it was verified to have a high-processing accuracy and efficiency for squint spotlight ASRW-SAR data. Finally, conclusions are summarized in Sec. 5.

2 Airborne Squint Spotlight Synthetic Aperture Radar Using Adaptive Sliding Receive-Window Technique

Figure 1 shows the acquisition geometry of squint spotlight SAR. We define the rectangular coordinate system $OXYZ$: the origin is the nadir at azimuth beginning time, the x-axis is parallel to the flight path and points along the azimuth direction, the y-axis is perpendicular to the x-axis on the ground and points along the range direction, and the z-axis provides a right-hand Cartesian coordinate system. As shown in Fig. 1, radar S is at $(x, 0, H)$, moving at speed v. φ is the squint angle, r is the reference range, and x is the function of the azimuth time t which indicates the position of the airplane along the azimuth direction. C is the scene center and A is a certain target in the scene. Also, the azimuth distance between the scene center C and target A is x_A, where $x_A = vt_A$. $R(t)$ denotes the instantaneous slant-range distance from the antenna phase center to a certain target A.

Combining all the geometry, the instantaneous slant-range distance $R(t)$ can be written as[1,9]

$$R(t) = \sqrt{r^2 + v^2(t - t_A)^2 - 2rv(t - t_A)\sin\varphi} = r - v(t - t_A)\sin\varphi + \frac{v^2(t - t_A)^2\cos^2\varphi}{2r} + \cdots$$

$$= r + \underbrace{\frac{\lambda}{2}f_d(t - t_A)}_{\text{range} - \text{walk}} + \underbrace{\frac{\lambda}{4}f_r(t - t_A)^2}_{\text{range} - \text{curve}} + \cdots,$$
(1)
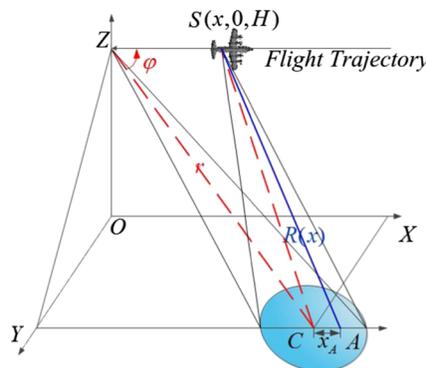
Fig. 1 Acquisition geometry of airborne squint spotlight synthetic aperture radar (SAR) mode.
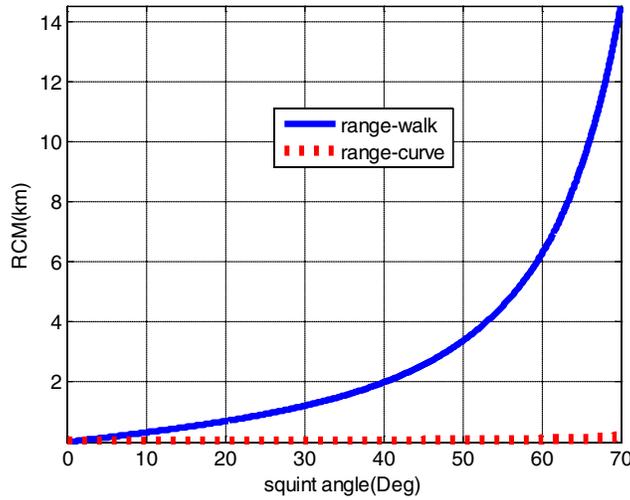
Fig. 2 Range cell migration (RCM) variation as a function of squint angle.

where λ is the signal wavelength and $f_d = -2v \times \sin \varphi / \lambda$ and $f_r = 2v^2 \cos^2 \varphi / (\lambda r)$ are referred to as the Doppler centroid and Doppler rate, respectively.[9] Figure 2 shows range-walk and range-curve variations as a function of the squint angle using the SAR system parameters listed in Table 1 (in Sec. 4). As range-walk is the prominent part of RCM in squint SAR, the removal of range-walk can be considered as the law of the ASRW technique. Also, the receive-window starting time has been changed as follows:

$$\Delta T(t) = 2 \cdot \frac{\frac{\lambda}{2} f_d (t - t_A)}{c} = \frac{2v(t - t_A) \sin \varphi}{c} = \frac{2(x - x_A) \sin \varphi}{c}, \qquad (2)$$

where c is the velocity of light and $x = vt$.

Figure 3 shows the operation mechanism for airborne squint spotlight SAR using the ASRW technique. The geometry of the squint spotlight SAR operating mode is demonstrated in Fig. 3(a). Also, the echo from the target can be received by sliding the receive window as the red lines show in Fig. 3(b). However, if the receive window is fixed, as the green lines in Fig. 3(c) show, the RCM closes to the receive window and the receive window must be long enough to receive all the RCM. As the RCM increases with high resolution and squint angle, the RCM may be outside the receive window. Figure 3(d) shows both of the two modes' SAR echoes in two-dimensional (2-D) signal processor memory, and the red lines illustrate that the RCM is reduced. As the range-walk is removed, the RCM is reduced significantly. This implies that the ASRW technique reduces the received echo data volume and saves the storage. Besides, most of the reduced echo data are invalid for the RCM, which would not affect the final imaging results. From the view of information entropy, the ASRW technique

Table 1 Synthetic aperture radar (SAR) parameters.

Parameter	Value	Parameter	Value
λ	1.0 cm	H	8000 m
v	150 m/s	Pulse repetition frequency (PRF)	600 Hz
f_s	1.7 GHz	r	30.9 Km
φ	40 deg /70 deg	D	0.6 m
τ	2 μs	f_c	30.0 GHz

(c) Receive time with fixed receive window

(b) Receive time with sliding receive window

(d) SAR echo in 2D signal processor memory

(a) Geometry of squint spotlight SAR
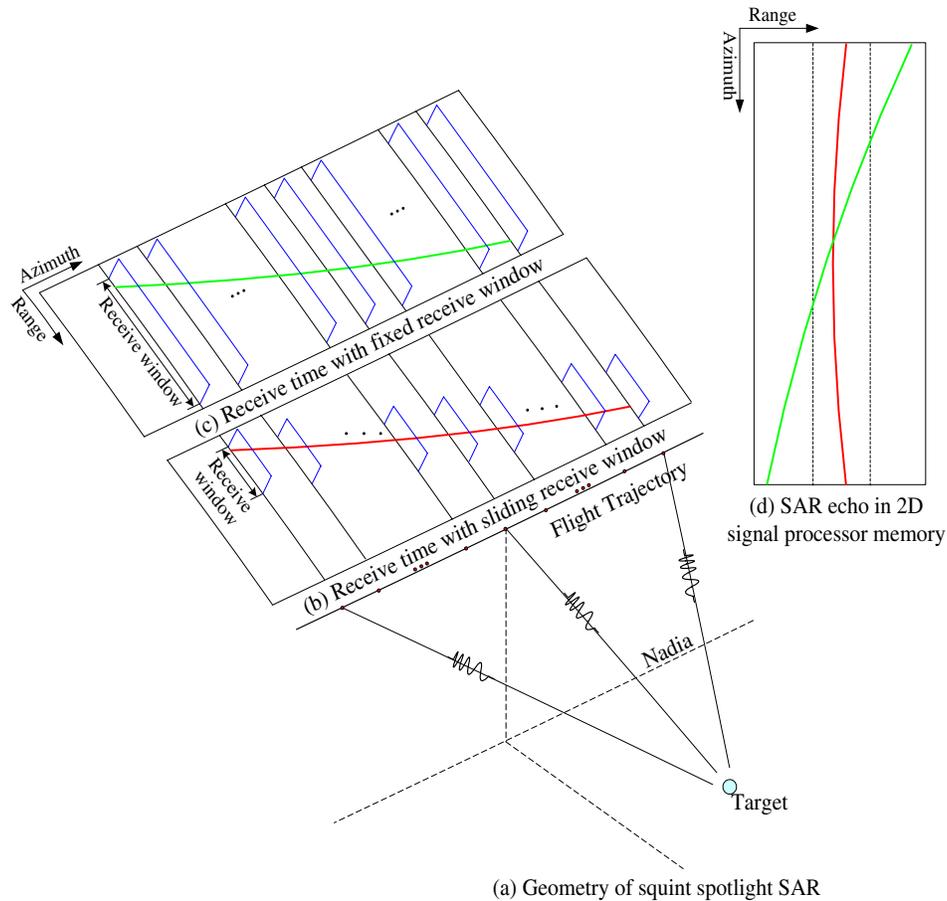
Fig. 3 Operation mechanism for airborne squint spotlight SAR using adaptive sliding receive window (ASRW).

actually performs a lossless compression in the data acquisition stage. Therefore, the ASRW technique has no adverse effect on the final imaging.

However, the receive window should start at the specified range of the sampling time due to the radar hardware design principle. This implies that the receive-window starting time is discrete

$$\Delta T_{\mathrm{dig}}(t) = \left\lfloor \frac{\Delta T(t)}{1/f_s} \right\rfloor \cdot f_s, \tag{3}$$

where $\lfloor \cdot \rfloor$ is an integral function. Also, a time-shift of the starting time results from $\Delta T_{\mathrm{dig}}(t)$ is given by

$$\Delta T_{\mathrm{shift}}(t) = \Delta T(t) - \Delta T_{\mathrm{dig}}(t). \tag{4}$$

So, the phase error, caused by $\Delta T_{\mathrm{shift}}(t)$, can be compensated for by Eq. (5) before the imaging focusing process. Then, the continuous variable $\Delta T(t)$ will still be used in the subsequent mathematical derivation

$$\Omega_1(f_\tau, t) = \exp\{j2\pi f_\tau \cdot \Delta T_{\mathrm{shift}}(t)\}, \tag{5}$$

where f_τ is range frequency.

3 Adaptive Sliding Receive-Window Synthetic Aperture Radar Fast Image-Formation Algorithm

Three components were proposed in this section: First, the expression of 2-D matched filtering function in the wave number domain was derived in detail. Then, based on the principle of WDA, a new Stolt-mapping relationship was illustrated according to the 2-D matched filtering function. Finally, a presentation of the process flow of the fast image-formation algorithm was given, which was proven to focus the ultrahigh-resolution airborne squint spotlight ASRW-SAR data accurately and efficiently.

3.1 Two-Dimensional Matched Filtering Function

In the subsequent analysis, the antenna beam pattern, backscatter coefficient, and other nonessential amplitude factors have been corrected. So, the point-target spectrum of the innovative mode can be given by

$$S(\tau, x) = p\left[\tau - \frac{2R(x)}{c} - \frac{2(x - x_A)\sin \varphi}{c}\right] \cdot \exp\left\{-j\pi b\left[\tau - \frac{2R(x)}{c} - \frac{2(x - x_A)\sin \varphi}{c}\right]^2\right\}$$
$$\cdot \exp\left\{-j\frac{4\pi R(x)}{\lambda}\right\}, \tag{6}$$

where $p[\cdot]$ is the signal envelope, b is the range chirp FM rate, and τ is the range time. Simply put, after range compression, the 2-D matched filtering function signal $h_r(\tau, x)$ is given by adopting the impulse response function instead of the sinc function as follows:

$$h_r(\tau, x) = \delta\left(\tau - \frac{2\Delta R(x)}{c} - \frac{2(x - x_A)\sin \varphi}{c}\right) \cdot \exp\left(-j\frac{4\pi f_c \Delta R(x)}{c}\right), \tag{7}$$

where $\Delta R(x) = R(x) - r$ and f_c denotes the carrier frequency. Because the position of the range-compressed signal is changed with $\Delta T(t)$, the wave number distribution varied accordingly. By applying the principle of stationary phase (POSP) to Eq. (7), $h_r(\tau, x)$ is changed from the range time domain to the range frequency domain

$$h_r(f_\tau, x) = \exp\left\{-j4\pi \frac{f_c + f_\tau}{c}(\Delta R(x) + x\sin \varphi)\right\} \cdot \exp\left\{j4\pi \frac{f_c}{c} x\sin \varphi\right\} \cdot \exp\{j\Phi_1(f_\tau, x_A)\}, \tag{8}$$

where $\Phi_1(f_\tau, x_A) = 4\pi f_\tau x_A \sin \varphi/c$. As $\Phi_1(f_\tau, x_A)$ is independent of x, it can be compensated for by a matched filter in the range frequency and azimuth time domain. Therefore, $h_r(f_\tau, x)$ can be rewritten after compensation as follows:

$$h_r(f_\tau, x) = \exp\left\{-j4\pi \frac{f_c + f_\tau}{c}(\Delta R(x) + x\sin \varphi)\right\} \cdot \exp\left\{j4\pi \frac{f_c}{c}\sin \varphi\right\}, \tag{9}$$

where the azimuth wave number $k_x = 2\pi f_a/v$, $k_0 = 2\pi f_d/v$, the range wave number $k_{rc} = 4\pi(f_c + f_\tau)/c$, and f_a is the Doppler frequency. Then, the signal $h_r(f_\tau, x)$ is converted to the range frequency and azimuth wave number domain

$$H_r(f_\tau, k_x) = \int \exp\{-jk_{rc}(\Delta R(x) + x\sin \varphi)\} \cdot \exp\left\{-j2\pi f_d \frac{x}{v}\right\} \exp\{-jk_x x\}dx. \tag{10}$$

Substituting $k_0 = 2\pi f_d/v$ into Eq. (10),

$$H_r(f_\tau, k_x + k_0) = \int \exp\{-jk_{rc}(\Delta R(x) + x\sin \varphi)\} \cdot \exp\{-j(k_x + k_0)x\}dx. \tag{11}$$

In squint mode, the center of the azimuth wave number is $-k_0 x$, and $k_x \in [-\pi(f_{PRF} - f_d)/v$ and $\pi(f_{PRF} - f_d)/v$] in Eq. (11), where f_{PRF} is equal to PRF. By using variable substitution, Eq. (11) can be written as follows:

$$H_r(f_\tau, k_x) = \int \exp\{-jk_{rc}(\Delta R(x) + x \sin \varphi)\} \cdot \exp\{-jk_x x\} dx, \tag{12}$$

where $k_x \in (-\pi f_{PRF}/v, \pi f_{PRF}/v)$. Then, by using POSP, the stationary phase point x_0 is given by

$$x_0 = r \sin \varphi - \frac{(k_{rc} \sin \varphi + k_x) r \cos \varphi}{\sqrt{k_{rc}^2 - (k_{rc} \sin \varphi + k_x)^2}} - x_A. \tag{13}$$

So, the expression of the 2-D matched filtering function in the range frequency domain and azimuth wave number domain is

$$H_r(f_\tau, k_x) = \exp\{-jr[\cos \varphi \sqrt{k_{rc}^2 - (k_{rc} \sin \varphi + k_x)^2} + \sin \varphi(k_{rc} \sin \varphi + k_x) - k_{rc}]\}. \tag{14}$$

Then, taking FFT of Eq. (14) with respect to r, we can get the expression of the 2-D matched filtering function in the wave number domain as

$$H_r(k_r, k_x) = \delta(k_r + [\cos \varphi \sqrt{k_{rc}^2 - (k_{rc} \sin \varphi + k_x)^2} + \sin \varphi(k_{rc} \sin \varphi + k_x) - k_{rc}]). \tag{15}$$

3.2 New Stolt-Mapping Relationship

Several modified Stolt-mapping relationships have been proposed in Refs. 14 and 15, which rewrite the expression of RCM. But they do not essentially change the mapping relationship between the frequency domain and wave number domain. For the image-formation algorithm of the squint spotlight ASRW-SAR, a new mapping relationship should be found immediately due to the sliding receive window. Assuming the range compress signal is $p(f_\tau, k_x)$, an IFFT was implemented with respect to f_τ after the matched filtering operation

$$P(r, k_x) = \int p(f_\tau, k_x) H_r^*(f_\tau, k_x) \exp\left(j \frac{4\pi f_\tau}{c} r\right) df_\tau, \tag{16}$$

where $H_r^*(f_\tau, k_x)$ is the complex conjugate of $H_r(f_\tau, k_x)$. Then, by applying FFT with respect to r

$$\begin{aligned} P(k_r, k_x) &= \iint p(f_\tau, k_x) \cdot H_r^*(f_\tau, k_x) \cdot \exp\left(j \frac{4\pi f_\tau}{c} r\right) \cdot \exp(-jk_r r) dr df_\tau \\ &= \int p(f_\tau, k_x) H_r^*\left(\frac{4\pi f_\tau}{c} - k_r, k_x\right) df_\tau. \end{aligned} \tag{17}$$

Substituting Eq. (15) into Eq. (17),

$$\begin{aligned} P(k_r, k_x) = \int \delta\Bigg(k_r - \Bigg[&\cos \varphi \sqrt{k_{rc}^2 - (k_{rc} \sin \varphi + k_x)^2} + \sin \varphi(k_{rc} \sin \varphi + k_x) - \frac{4\pi f_c}{c}\Bigg]\Bigg) \\ &\cdot p(f_\tau, k_x) df_\tau. \end{aligned} \tag{18}$$

So, a new mapping relationship is illustrated as follows

$$k_r = \cos \varphi \sqrt{k_{rc}^2 - (k_{rc} \sin \varphi + k_x)^2} + \sin \varphi(k_{rc} \sin \varphi + k_x) - \frac{4\pi f_c}{c}. \tag{19}$$

According to the new mapping relationship, it is easy to convert $p(f_\tau, k_x)$ from the range frequency domain to the 2-D wave number domain $p(k_r, k_x)$ by interpolation. Finally,

fine-focusing the image can be done using the azimuth IFFT, geometric correction, and range IFFT operation.

3.3 *Processing Scheme of Fast Image-Formation Algorithm*

As Fig. 4 shows, the processing steps of the fast image-formation algorithm are divided into six stages as follows: time-shift compensation, azimuth deramping, data transform, bulk compression, modified Stolt mapping, and geometric correction.

As analyzed in Sec. 2, the time-shift $\Delta T_{\text{shift}}(t)$ causes a phase error. So, the first step of the proposed algorithm is to compensate for the phase error as in Eq. (5).

The overlapped azimuth spectrum limits the direct application of the available stripmap imaging algorithm in the spotlight SAR mode. To resolve the problem, azimuth deramping is adopted to eliminate the azimuth spectrum aliasing. Azimuth deramping shares the same processing flow as in Ref. 16.

The data transform stage includes four processing steps, namely, range FFT, phase compression, azimuth FFT, and residual phase compensation. For ASRW-SAR, the receive-window starting time is changed pulse-by-pulse in the azimuth direction. So, the Doppler history is variable in azimuth, which means that the target located only in the scene center is precisely focused. As analyzed in Sec. 3.1, in order to guarantee the focusing accuracy of all the targets located in different azimuth positions, the third exponential phase term in Eq. (8) should be compensated for, which is given by

$$\Omega_2(f_\tau, x) = \exp\left\{-j\frac{4\pi f_\tau x_A \sin \varphi}{c}\right\}. \tag{20}$$

Only the targets apart from the scene center at the distance x_A in azimuth direction will be precisely focused. To ensure the imaging quality over the whole scene, a method based on block
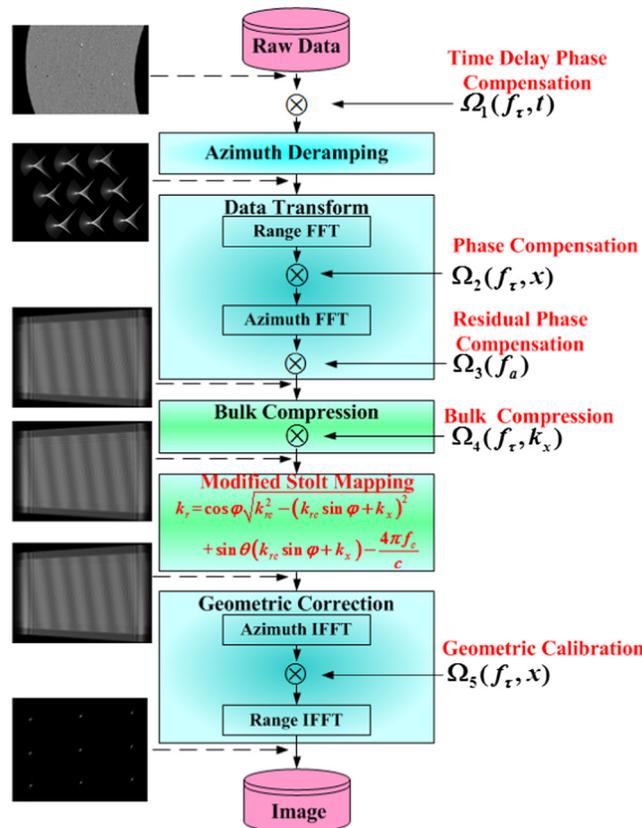
Fig. 4 Flowchart of the proposed wave number domain algorithm (WDA).
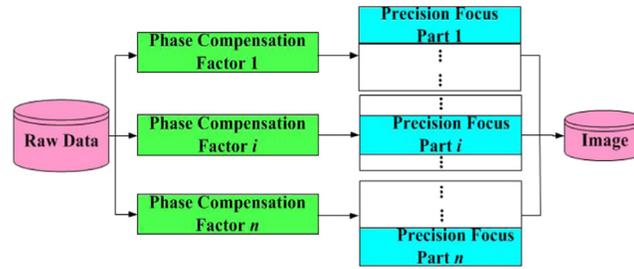
Fig. 5 Flowchart of block processing.

processing was proposed in Fig. 5. Echo data can be divided into n blocks along the azimuth direction, and each block can be compensated for by using different x_A values.

Moreover, after performing the azimuth FFT, the residual phase caused by azimuth deramping processing[16] should be compensated for by

$$\Omega_3(f_a) = \exp\left\{j\pi\frac{f_a^2}{f_r}\right\}. \tag{21}$$

In the bulk compensation stage, the reference function is different from the traditional function in Ref. 1. Therefore, in a practical procedure, the reference function in bulk compensation is given by

$$\Omega_4(f_\tau, k_x) = \exp\{jr \cdot \cos\varphi\sqrt{k_{rc}^2 - (k_{rc}\sin\varphi + k_x)^2} + \sin\varphi(k_{rc}\sin\varphi + k_x)\}$$
$$\cdot \exp\left\{-j\pi\frac{f_\tau^2}{b}\right\} \cdot \exp\left\{-j\frac{4\pi f_\tau r_{min}}{c}\right\}, \tag{22}$$

where r_{min} is minimum slant range, $r_{min} = r - c \cdot N_r/(2f_s)$, and N_r denotes the range resample point. In Eq. (22), the first exponential term compensates for the phase at the reference slant range as the 2-D matched filtering function $H_r(f_\tau, k_x)$ shows in Eq. (14). The second exponential term finishes the range compression and the third exponential term allows for redundant phase compensation, which are all caused by digital processing. After the bulk compression, the target at the reference range is properly focused, but a residual phase still exists for the targets at other ranges.

Different from the conventional Stolt mapping, the proposed Stolt mapping is modified as in Eq. (19) due to the change in the data-mapping relationship caused by the ASRW technique. The modified Stolt mapping performs the differential RCMC, differential SRC, and differential azimuth compression. After the modified Stolt mapping processing, the whole scene is acurately focused.

The last processing part is the geometric correction, which compensates for the change in the receive-window starting time caused by the ASRW technique. After the modified Stolt mapping, the azimuth IFFT is performed to transform the data into the azimuth time and range frequency domain. After that, geometric distortion is corrected by

$$\Omega_5(f_\tau, x) = \exp\left\{j4\pi f_\tau\frac{\sin\varphi}{c}x\right\}. \tag{23}$$

Finally, a range IFFT is applied to get the fine-focusing and a nondistorted SAR image.

4 Experimental Results

In this section, a Ka-band linear frequency modulation transmission signal is adopted for simulation, and the azimuth resolution ρ_a is 0.1 m. First, to prove the effectiveness of the ASRW technique, the experiments comparing the raw echo between the ASRW-SAR and conventional-SAR are carried out. Then, to verify the validity of the proposed image-formation algorithm,
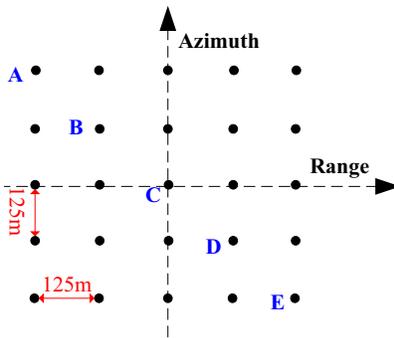
Fig. 6 Simulation scene.

the experiments with point targets imaging experiments are carried out. The specific simulation parameters are listed in Table 1, and the simulation scene ($500 \times 500 \text{ m}^2$, resulting in 5000×5000 pixels in the SAR image) is illustrated by Fig. 6.

In ASRW-SAR, the ASRW technique changes the starting time of the receive window in each azimuth direction by removing the range-walk. Also, the length of the range dimension is dependent on the RCM, whose main part is range-walk. Figure 7 shows the raw echo data of ASRW-SAR and conventional-SAR systems at different squint angles ($\varphi = 40 \text{ deg}/70 \text{ deg}$). Also, the range sample number in a conventional-SAR and ASRW-SAR are N_r and N_r', respectively. As shown in Fig. 7, the RCM is reduced by ASRW, and the range sampling number decreases significantly. Further, the higher the squinted angle, the bigger the range sampling number scaling and the more immediate the demand of ASRW.

In the imaging experiments part, the imaging results of a conventional WDA and the proposed imaging algorithm are shown in Fig. 8. The comparison results of the proposed imaging algorithm with a conventional WDA shows that the proposed method is effective. Also, Figs. 9 and 10 show the interpolated contour plots of the corresponding focusing targets A, C, and E in different squint angles. The spatial resolution (azimuth resolution ρ_a, range resolution ρ_r), peak side lobe ratio, and integrated side lobe ratio of the three
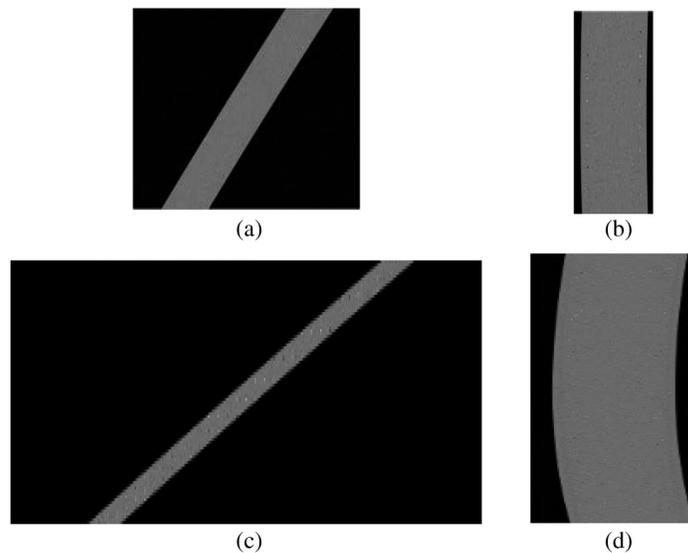
Fig. 7 Comparing the echo data of ASRW-SAR and conventional SAR systems at different squint angles. (a) conventional SAR, $\varphi = 40 \times \text{deg}$, Nr = 32768, (b) ASRW SAR, $\varphi = 40 \times \text{deg}$, Nr =8192, (c) conventional SAR, $\varphi = 70 \times \text{deg}$, Nr = 262144, and (d) ASRW SAR, $\varphi = 70 \times \text{deg}$, Nr = 16384.
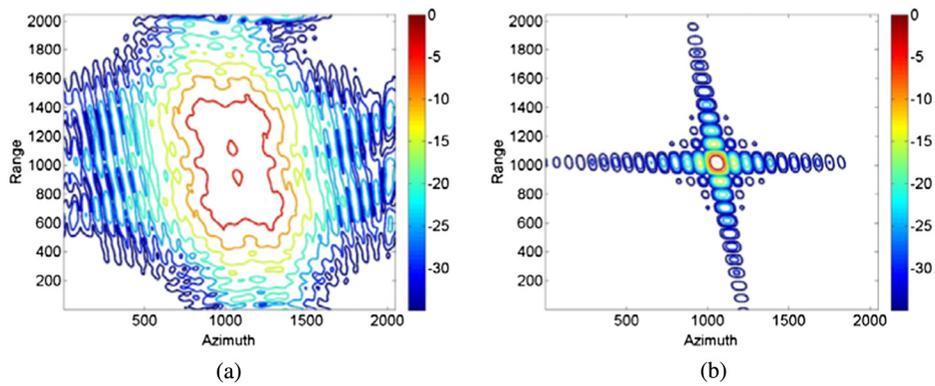
Fig. 8 Comparing imaging results of conventional WDA and improved algorithm. (a) Conventional WDA. (b) Proposed imaging algorithm.
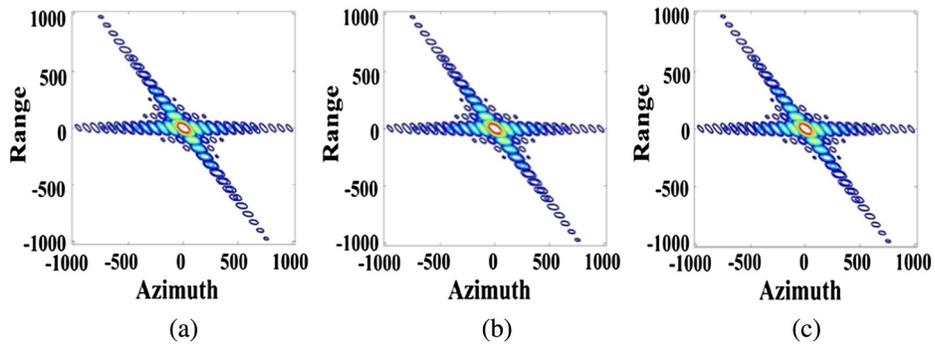
Fig. 9 Imaging results of the improved algorithm in $\varphi = 40$ deg. (a) Target A. (b) Target C. (c) Target E.
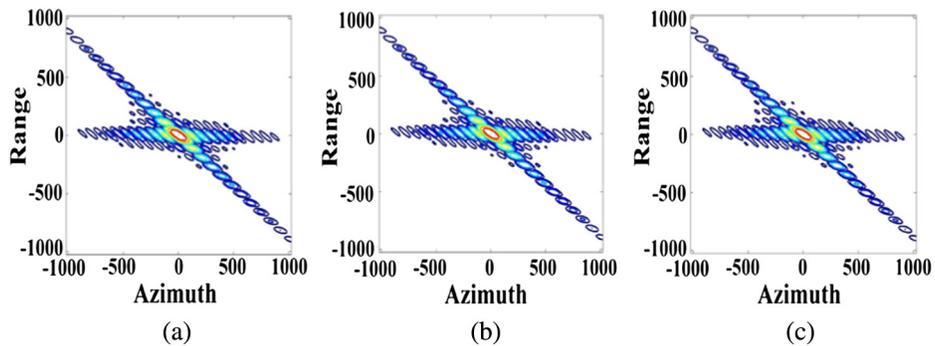
Fig. 10 Imaging results of the improved algorithm in $\varphi = 70$ deg. (a) Target A. (b) Target C. (c) Target E.

point targets processing results are listed in Table 2. Both the contour plots and image evaluation results demonstrate that the fine-focusing performance of the proposed improved image-formation algorithm and all the evaluation results indicate that the image results are slightly affected by the spatial variant slant range. Besides, the comparison of the computation load of conventional-SAR and ASRW-SAR is represented in the Appendix, and the computation efficiency is $\gamma = 4.1/17.0$ in $\varphi = 40$ deg$/70$ deg. The advantage of less-computation load indicates its potential suitability in a real-time imaging system.

ρ_r^* denotes the slant range resolution.

Table 2 Targets A, B, and C evaluation results in different squint angles.

			Azimuth			Range	
		ρ_a (m)	Peak side lobe ratio (PSLR) (dB)	Integrated side lobe ratio (ISLR) (dB)	ρ_r^* (m)	PSLR (dB)	ISLR (dB)
	A	0.100	−13.28	−10.28	0.089	−13.30	−10.12
	B	0.100	−13.26	−10.27	0.089	−13.30	−10.12
$\varphi = 40$ deg	C	0.100	−13.26	−10.27	0.089	−13.30	−10.12
	D	0.100	−13.26	−10.27	0.089	−13.30	−10.12
	E	0.100	−13.27	−10.28	0.089	−13.30	−10.12
	A	0.102	−12.88	−9.62	0.088	−13.32	−10.39
	B	0.101	−12.86	−9.63	0.087	−13.31	−10.39
$\varphi = 70$ deg	C	0.101	−12.85	−9.64	0.087	−13.31	−10.39
	D	0.101	−12.87	−9.62	0.087	−13.31	−10.39
	E	0.103	−12.89	−9.61	0.088	−13.32	−10.38

5 Conclusion

In this article, an ASRW technique was introduced for efficiently acquiring the airborne highly squint spotlight SAR echo. The airborne squint spotlight ASRW-SAR varies its receive-window starting time pulse-by-pulse as a function of range-walk, namely, the linear term of RCM. So, the RCM of ASRW-SAR is reduced dramatically and the range sampling number is decreased, which means the data volume and the computation loads are reduced. Therefore, the ASRW technique decreases the SAR system complexity, and has great potential value in real-time imaging systems.

In order to deal with the varying receive-window starting times in airborne squint spotlight ASRW-SAR, a fast image-formation algorithm is presented for highly precise focusing of the ultrahigh-resolution (e.g., 0.1 m) airborne squint spotlight ASRW-SAR data. First, azimuth deramping preprocessing is performed to eliminate the azimuth spectrum aliasing. Then, bulk compression and modified Stolt mapping are utilized for precise focusing. At last, geometric correction is implemented to remove the effect of the varying receive-window starting time by the ASRW technique. The validity and accuracy of the proposed algorithm have been demonstrated by point targets simulation data. Also, the processing results of point targets at different squint angles indicate that the proposed algorithm is suitable for high-resolution and high squint angle airborne spotlight SAR image formation. Further, the computation load is reduced, which would be more markedly decreased in high squint angle, e.g., 17 times improvement of computation efficiency at a 70-deg squint angle.

Appendix: Comparison of Computation Load of Conventional-SAR and ASRW-SAR

The number of multiplications is adopted as a computation load indicator. Let the interpolation kernel length be M_{ken}. Also, the azimuth sample numbers in conventional SAR and ASRW-SAR are N_a and N_a', respectively. The particular computational load in each imaging stage is listed in Table 3.

C_{con} denotes the entire computational load for conventional-SAR.

$$C_{\text{con}} = (12 + 2M_{\text{ken}})N_a N_r + 6N_a N_r \log_2 N_a + 4N_a N_r \log_2 N_r. \tag{24}$$

Table 3 Computation load comparison.

	Conventional SAR	ASRW-SAR
Azimuth deramping	$8N_aN_r + 2N_aN_r\log_2 N_a$	$8N_a'N_r' + 2N_a'N_r'\log_2 N_a'$
Range FFT	$2N_aN_r\log_2 N_r$	$2N_a'N_r'\log_2 N_r'$
Azimuth FFT	$2N_aN_r\log_2 N_a$	$2N_a'N_r'\log_2 N_a'$
Bulk compression	$4N_aN_r$	$4N_a'N_r'$
Stolt mapping	$2M_{\mathrm{ken}}N_aN_r$	$2M_{\mathrm{ken}}N_a'N_r'$
Azimuth IFFT	$2N_aN_r\log_2 N_a$	$2N_a'N_r'\log_2 N_a'$
Geometric correction	0	$4N_a'N_r'$
Range IFFT	$2N_aN_r\log_2 N_r$	$2N_a'N_r'\log_2 N_r'$

Also, the entire computational load C_{ASRW} for ASRW-SAR is expressed as

$$C_{\mathrm{ASRW}} = (16 + 2M_{\mathrm{ken}})N_a'N_r' + 6N_a'N_r'\log_2 N_a' + 4N_a'N_r'\log_2 N_r'. \qquad (25)$$

Assume that the computational efficiency γ is defined as

$$\gamma = \frac{C_{\mathrm{con}}}{C_{\mathrm{ASRW}}}. \qquad (26)$$

With the condition of the same parameters as listed in Table 1, N_a and N_a' are equivalent, $N_a = N_a' = [(v \cdot \mathrm{PRF})/(\rho_a \cdot f_r)]$ assuming an 8-point interpolation is adopted ($M_{\mathrm{ken}} = 8$). And in different squint angle $\varphi = 40$ deg$/70$ deg, N_a (or N_a') is equal to 17,500/87,792. Also, the N_r and N_r' are listed in Fig. 6 in different squint angles. Therefore, the computation efficiency γ is calculated by Eq. (26) in different squint angles, and the final value γ is listed in Table 2.

Acknowledgments

References

1. I. G. Cumming and F. H. Wong, *Digital Processing of Synthetic Aperture Radar Data: Algorithms and Implementation*, Artech House, Norwood, Massachusetts (2005).
2. S.-I. Hwang, H. Wang, and K. Ouchi, "Comparision and evaluation of ship detection and identification alogrithms using small boats and ALOS-PALSAR," *IEICE Trans. Commun.* **E92-B**(12), 3883–3892 (2009).
3. H. Ang et al., "Assessment of building damage in 2008 wenchuan earthquake from multi-temporal SAR images using getis statistic," *IEICE Trans. Commun.* **E94-B**(11), 2983–2986 (2011).
4. S. Cimmino et al., "Efficient spotlight SAR raw signal simulation of extended scenes," *IEEE Trans. Geosci. Remote Sens.* **41**, 2329–2337 (2003).
5. G.W. Davidson and I. Cumming, "Signal properties of spaceborne squint-mode SAR," *IEEE Trans. Geosci. Remote Sens.* **35**(3), 611–617 (1997).
6. V. C. Koo et al., "A new unmanned aerial vehicle synthetic aperture radar for environmental monitoring," *Prog. Electromagn. Res.* **125**, 527–543 (2012).

7. D. Reale et al., "Advanced techniques and new high resolution SAR sensors for monitoring urban areas," in *Geoscience and Remote Sensing Symposium (IGARSS), 2010 IEEE International*, Honolulu, HI, pp. 1800–1803 (2011).
8. H. Cheng, T. Long, and Y. Tian, "An improved nonlinear chirp scaling algorithm based on curved trajectory in geosynchronous SAR," *Prog. Electromagn. Res.* **135**, 481–513 (2013).
9. D. X. An et al., "Extended nonlinear chirp scaling algorithm for high-resolution highly squint SAR data focusing," *IEEE Trans. Geosci. Remote Sens.* **50**(9), 3595–3609 (2012).
10. Y. Wang, O. Loffeld, and S. Knedlik, "Spotlight-mode SAR data focusing using a modified wavenumber domain algorithm," in *Geoscience and Remote Sensing Symposium, IGARSS*, pp. 567–570 (2007).
11. H.-S. Shin and J.-T. Lim, "Omega-k algorithm for spaceborne spotlight SAR imaging," *IEEE Geosci. Remote Sens. Lett.* **9**(3), 343–347 (2012).
12. L. Riccardo et al., "Spotlight SAR data focusing based on a two-step processing approach," *IEEE Trans. Geosci. Remote Sens.* **39**(9), 1993–2004 (2001).
13. R. Bamler, "A comparision of range-Doppler and wavenumber domain SAR focusing algorithm," *IEEE Geosci. Remote Sens.* **30**(4), 706–713 (1992).
14. M. Vandewal, R. Speck, and H. Sub, "Efficient and precise processing for squinted spotlight SAR through a modified stolt mapping," *EURSAIP J. Adv. Signal Process.* **2007**(1), 33–39 (2007).
15. A. Reigber, E. Alivizatos, and A. Potsis, "Extended wavenumber domain synthetic apeture radar focusing with integrated motion compensation," *IEEE Proc., Sonar Navig.* **153**(3), 301–310 (2006).
16. D. Guo, H. Xu, and J. Li, "Extended wavenumber domain algorithm for highly squinted sliding spotlight SAR data processing," *Prog. Electromagn. Res.* **114**, 17–32 (2011).

Wei Yang received the MS and PhD degrees from Beihang University, China, in 2008 and 2011, respectively. He has been a lecturer with the School of Electronics and Information Engineering, Beihang University, since 2013. His current research interests include high-resolution spaceborne SAR image formation and modeling and simulation for spaceborne SAR systems.

Hong-cheng Zeng received the BS degrees in college of Information and Electrical Engineering from China Agriculture University in 2011. He is currently working towards his PhD at Beihang University. His research interest is high-resolution spaceborne SAR image formation.

Jie Chen received the BS and PhD degrees from Beihang University, China, in 1996 and 2002, respectively. He is a professor with the School of Electronics and Information Engineering, Beihang University (BUAA) from 2004. His current research interests include remote sensing information acquisition and signal processing; topside ionosphere exploration based on spaceborne HF-SAR; high-resolution spaceborne SAR image formation; modeling and simulation for spaceborne SAR systems.

Peng-bo Wang received the PhD degrees from Beihang University (BUAA), China, in 2007. He has been a lecturer with the School of Electronics and Information Engineering, Beihang University, since 2010. His current research interests include remote sensing information acquisition and signal processing; high-resolution spaceborne SAR image formation; modeling and simulation for spaceborne SAR systems.